



# In situ investigation of MgO nanocube deformation at room temperature

I. Issa,<sup>a,b</sup> J. Amodeo,<sup>a,\*</sup> J. Réthoré,<sup>b</sup> L. Joly-Pottuz,<sup>a</sup> C. Esnouf,<sup>a</sup> J. Morthomas,<sup>a</sup> M. Perez,<sup>a</sup>  
J. Chevalier<sup>a</sup> and K. Masenelli-Varlot<sup>a</sup>

<sup>a</sup>Université de Lyon, INSA-Lyon, MATEIS, CNRS UMR5510, 69621, France

<sup>b</sup>Université de Lyon, INSA-Lyon, LAMCOS, CNRS UMR5259, F-69621 Villeurbanne Cedex, France

Received 12 September 2014; revised 13 November 2014; accepted 1 December 2014

Available online 12 January 2015

**Abstract**—The mechanical behavior of (100)-oriented MgO nanocubes is investigated using in situ transmission electron microscopy (TEM) compression tests at room temperature and molecular dynamics simulations. Experiments show high strength and ductility, in addition to specific deformation mechanisms interpreted by the simulation. The nucleation and the propagation of  $1/2(110)\{110\}$  dislocations are at the onset of the plastic deformation. The different deformation processes as well as the possible formation of a dislocation network during compression are discussed. © 2014 Acta Materialia Inc. Published by Elsevier Ltd. All rights reserved.

**Keywords:** MgO; In situ TEM; Nanoparticles; Molecular dynamics; Nanomechanics

## 1. Introduction

Nanocrystalline (NC) ceramics are of particular interest because of their high mechanical characteristics (e.g. high hardness, crack propagation resistance and superplastic deformation at moderate temperatures), which are better than their conventional polycrystalline counterparts [1,2]. Therefore, NC ceramics are increasingly used for their mechanical properties, as example in the field of modern orthopaedic surgery where they are employed as femoral heads or acetabular cups, in replacement of metallic alloys, to extend medical prosthesis lifetime. Their use indeed reduces wear rates and ion release, presumed to be responsible for inflammatory reactions [3,4]. In this context, one way to enhance the mechanical properties of post-processed NC ceramics and thereby optimize their compaction and sintering processes is to improve the global understanding of the mechanics of ceramic nanoparticles (NPs).

As for NC ceramics, the mechanical properties of nano-objects such as pillars, particles or wires have recently drawn intensive scientific attention, mainly through their high achievable yield strength and ductility [5]. Owing to the characteristic sizes of such objects, in situ mechanical tests in a transmission electron microscope (TEM) or in a scanning electron microscope (SEM) have revealed to give valuable pieces of information regarding the deformation mechanisms [6,7]. Deep in the submicrometer scale, size phenomena influence elastic properties of nanowires (NWs) and NPs through the combination of surface and

core effects in both the experiments and the atomistic simulations [8,9]. This size effect involves also the plastic deformation regime for whom few theories based on the single-arm dislocation source model or the dislocation nucleation/starvation model [10,11] still try to provide a unique description of the now well-known principle “smaller is stronger”. Nevertheless, most of these studies are carried on metals, especially face-centered cubic (fcc), and only few works have been dedicated to ceramics [12–15]. Calvie and collaborators have recently reported in situ compression tests in the TEM of a  $\gamma$ -alumina  $\text{Al}_2\text{O}_3$  nanospheres [14]. The main feature of this study is that the sample undergoes wide and homogeneous plastic deformation, as observed in metallic [16,17], intermetallic [18] or silicon [19,20] NPs. A detailed mechanical analysis based on digital image correlation (DIC) and finite element simulations allowed the determination of a mechanical constitutive law [21]. However, the identification of elementary mechanisms responsible for plastic deformation in  $\gamma$ - $\text{Al}_2\text{O}_3$  nanospheres could not be determined in situ. In particular, no dislocation could be observed experimentally. This lack was primarily attributed to the spherical geometry of the sample and to the diffraction conditions. Furthermore,  $\gamma$ - $\text{Al}_2\text{O}_3$  is not a stable phase at the macroscopic scale that restricts drastically the comparison of its mechanical properties to the other bulk-type alumina ( $\alpha$ -phase). At this point, it has to be mentioned that dislocations could successfully be observed in situ in silver NPs [22] but the compression axis could not be clearly determined from the images and the interpretation remained qualitative.

Here we propose to reach further the investigation of the mechanical behavior of single crystalline ceramic NPs using in situ TEM compression tests and molecular dynamics

\* Corresponding author. Tel.: +33 4 72 43 82 35; fax: +33 4 72 43 85 39; e-mail: [jonathan.amodeo@insa-lyon.fr](mailto:jonathan.amodeo@insa-lyon.fr)

(MD) simulations applied to magnesium oxide (MgO). MgO is an ionic ceramic with the B1 crystalline structure which has been widely studied in the past decades for its potential application as a refractory material ( $T_f > 3000$  K). MgO is also considered as a model material for dislocation properties analysis in B1-structured alkali halides and other ionic ceramics (e.g. NaCl, LiF, KCl, CaO, etc.) [23]. As most ceramic materials do under compression, bulk MgO single crystals accommodate only a slight amount of strain before failure ( $\sim 7\%$  for  $\langle 100 \rangle$ -oriented samples) at room temperature (RT), while larger deformation is reached at higher temperature [24,25]. In bulk MgO, plastic strain is governed by lattice friction, solution hardening or dislocation–dislocation interactions depending on the investigated temperature range [26–28]. At RT, lattice friction competes with solution hardening on the two main slip system families  $1/2\langle 110 \rangle\{110\}$  and  $1/2\langle 110 \rangle\{100\}$  of the crystalline structure.  $\{111\}$  and  $\{112\}$  slips have been observed only in rare and exotic cases [29–31].  $1/2\langle 110 \rangle\{110\}$  dislocation glide involves the nucleation of kink-pairs, typical of the lattice friction regime. This specific process leads to a characteristic dislocation microstructure made of rate-controlling long screw dislocations [32,33] which are also observed in body-centered cubic (bcc) metals at low temperature [34,35]. Above a transition temperature ( $\sim 600$  K for  $1/2\langle 110 \rangle\{110\}$  slip systems and  $1500$  K for  $1/2\langle 110 \rangle\{100\}$ ), lattice friction is overcome and plastic strain is accommodated by curved dislocations [36,37], ruled by the strength of dislocation–dislocation “forest” interactions [38,39]. In addition to well-known mechanical properties, MgO is stable at small scale and high pressure [40,41]. Finally, MgO NPs can be easily synthesized from different methods, leading to perfectly well-shaped nanocubes [42,43]. This sharp geometry permits us to easily define a standard  $[001]$  compression axis, simplify the identification of slip systems and reduce the misorientation troubles commonly observed in nanosphere compression tests.

In this study, we report in situ compression experiments in the TEM and MD compression simulations of MgO nanocubes at RT. Simulations are performed to investigate elementary deformation mechanisms at the atomic scale and corroborate experimental observations.

## 2. Materials and methods

### 2.1. Nanocube experimental synthesis and characterization

Magnesium oxide nanocubes were prepared by burning commercial magnesium chips (4–30 mesh) in air as described in the pioneer work of Heidenreich [44]. This specific method is known to produce perfectly cubic-shaped NPs down to sizes of a few nm. The smoke particles were caught directly on three substrates: a glass substrate for SEM imaging, a TEM grid (Cu 300-mesh covered by a holey carbon film) and the nanocompression sapphire substrate.

Primary characterizations were carried out by SEM, high resolution TEM (HRTEM) and weak beam dark field (WBDF) TEM. SEM images were acquired on a Zeiss Supra 55VP microscope. The acceleration voltage was fixed to 1 kV and images were acquired with a secondary electron Everhardt–Thornley detector. For the HRTEM

observations, a JEOL 2010F TEM microscope equipped with a field emission gun and operating at 200 kV was used. Images were recorded using a Gatan Orius 200 CCD camera. Energy-dispersive spectroscopy (EDS) was performed using an 80 mm<sup>2</sup> SSD detector from Oxford Instruments. Finally, WBDF characterizations were carried out on a JEOL 200CX microscope, equipped with a tungsten filament that operates at 200 kV. Images were acquired with the wave  $[220]$ , that allows the detection of dislocations in the  $(101)$ ,  $(10\bar{1})$ ,  $(011)$  and  $(01\bar{1})$  slip planes. Under such conditions, dislocations can be imaged as narrow lines which are approximately 10–15 nm wide [45].

A typical SEM image of the collected smoke is displayed Fig. 1a. Particles consist mostly of sharp nanocubes with edge sizes ranging between 20 nm and 300 nm. EDS spectra (not displayed) acquired during HRTEM observations indicate that the nanocubes are exclusively composed of MgO ( $99.9 \pm 0.1$  at.%). Particles are single crystals, as shown in the HRTEM image of Fig. 1b. The surfaces of the nanocubes are crystalline as well and are oriented along the  $\langle 100 \rangle$  directions, as shown by the electronic diffraction patterns, Fig. 1b. Regarding the importance that dislocations have during all stages of plastic deformation, a large number of MgO nanocubes were characterized by WBDF before any mechanical test. Fig. 1c displays a WBDF image of two MgO nanocubes. The image shows no bulk lattice defect such as dislocations, grain boundaries or twinning. Contrasts were only observed at the contact points of the nanocubes, and were attributed to the stress field induced by the elastic compression of the lattice [46]. None of the imaged nanocubes was found to contain bulk lattice defects. In the following, similar samples used for in situ nanocompression testing will thus be considered as initially dislocation-free.

### 2.2. In situ TEM nanocompression

Pristine MgO nanocubes were deposited onto a 75  $\mu\text{m}$  thick sapphire substrate by passing the substrate in the smoke during synthesis. This method precludes the use of solvents that may modify the surface structure of MgO samples [47]. Since the nanocubes exhibit  $\langle 100 \rangle$  surfaces, the compression axis is expected to be parallel to  $[001]$ .

In situ nanocompression tests were carried out using a dedicated sample holder from Nanofactory Instruments, fitted in a JEOL 2010F microscope operating at 200 kV accelerating voltage. The sample holder was equipped with a truncated diamond tip (flattened area of  $\sim 0.25 \mu\text{m}^2$ ) and a load cell (maximum load of 3 mN), as shown Fig. 1d. Particles were positioned on the substrate and displaced toward the tip during compression at a controlled displacement rate of  $2 \text{ nm s}^{-1}$ , which is equivalent to an engineering strain rate of  $0.02 \text{ s}^{-1}$  for a 100 nm nanocube.

The longitudinal displacement of the substrate was determined using DIC. For this purpose, a rigorous comparison of gray level transitions between the tip, the samples and the substrate has been performed on successive images. DIC allows arbitrary displacement fields to be estimated with a sub-pixel resolution ( $\sim 1/100$  pixel). The distance measured between substrate and diamond tip edges corresponds to the instant size of the sample. Furthermore, not only the longitudinal displacement but also the lateral deformation was obtained. As the longitudinal and lateral deformations were synchronized on-the-fly with the force

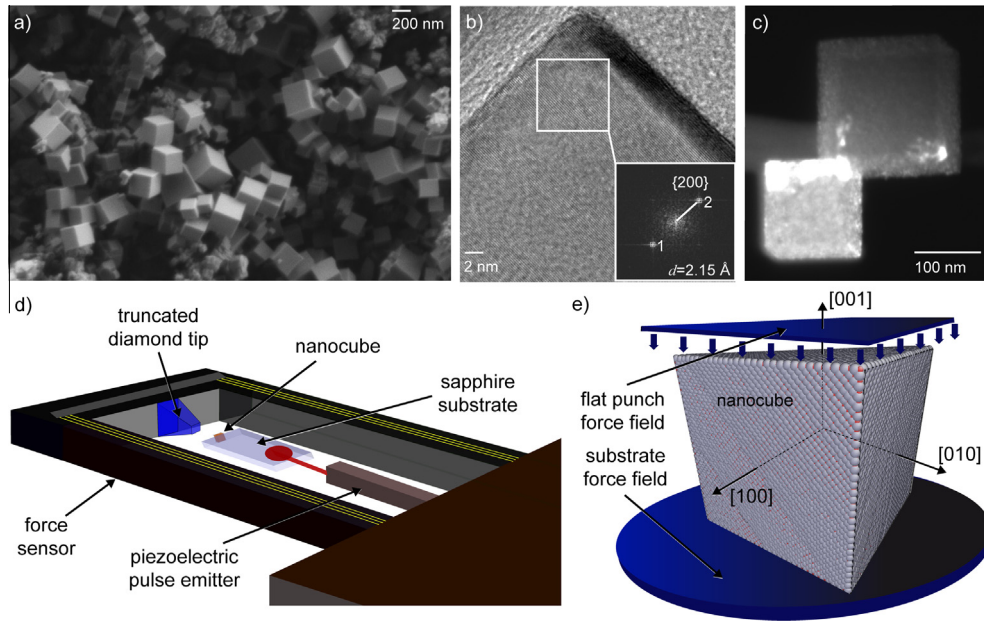


**Fig. 1.** (a) SEM image of smoked MgO nanocubes. (b) HRTEM image of a nanocube. In the inset, the diffraction pattern shows {200} crystallographic planes with a lattice spacing of  $\sim 2.15$  Å. The sample is fully crystalline and surfaces are oriented along the  $\langle 100 \rangle$  directions. (c) WBDF TEM image of two nanocubes free of bulk lattice defects. Only few contrasts due to contacts between adjacent cubes can be observed. (d) Scheme of the nanocompression experimental set-up. For the sake of clarity, the size of the sample has been widely increased compared to other components. (e) Scheme of the MD nanocompression simulation set-up, made of two force fields to respectively sustain and compress the nanocube.

value, true stress and true strain were deduced considering that lateral deformations were equivalent in both directions. The true strain is defined as  $\ln(L/L_0)$ , where  $L$  is the instantaneous position and  $L_0$  is the initial position of the substrate with respect to the tip, i.e. the initial nanocube size. The true stress is defined as the ratio between the instant force measured by the sensor and the effective cube surface inferred from the DIC calculation.

### 2.3. Computational methods

MD simulations were performed to investigate elementary deformation mechanisms of initially dislocation-free MgO nanocubes under compression at RT using the LAMMPS code [48]. Atomic interactions were described using a rigid ion model that included a Buckingham term in addition to long-range Coulombic interactions. Here we used the Ball and Grimes partial charges parameterization [49] successfully employed to describe surface diffusion [49], elastic constants and dislocation properties [50], which are considered as key points for interatomic potential transferability towards nanomechanical test simulations. We used a cut-off parameter of 8 Å for short-range interactions. Full long-range interactions between charges in compression simulations were computed using the multi-level summation method (MSM) solver [51]. MSM relative error in per-atom forces from  $10^{-4}$  to  $10^{-8}$  were tested without significant outcome on the simulation results. Cubic samples with edge lengths from 4.2 nm to 12.7 nm were shaped with free surfaces oriented along the  $\langle 100 \rangle$  directions, as suggested by the experiment. The MD compression tests of MgO nanocubes were performed using the following procedure. First, the structure of the nanocubes was optimized using conjugate gradient and the FIRE algorithm [52]. Next, the samples were equilibrated during 30 ps in the

NVE ensemble down to 300 K. Then, we used the Nosé–Hoover thermostat [53] for 50 ps equilibration in the NVT canonical ensemble. Finally, the compression tests were performed using two external potentials (see Fig. 1e) which model an infinite flat punch and the substrate [54,55]. To model uniaxial compression along the [001] direction, the top indenter was subjected to a constant displacement rate equivalent to an engineering strain rate of  $10^8 \text{ s}^{-1}$ . The bottom potential was kept fixed to sustain the sample. During compression simulations, time steps down to 2 fs were used and the Nosé–Hoover thermostat imposed a temperature of 300 K. Note that sample size, strain rate and other simulation parameters were chosen regarding settings generally adopted in the case of the embedded-atom method (EAM) for metals [17], which involves a significant increase of the cpu costs due to long-range Coulombic interactions in this study. The true strain was calculated as in the experiment (see previous section) and the compressive stress was computed as the ratio between the force experienced by the indenter and the instantaneous contact area drawn by the last upper atomic layers. Simulations were analyzed using *AtomViewer* [56], a tool which combines a modified bond-angle method [57] to identify crystalline structures, a Nye-tensor analysis for dislocation Burgers vector definition [58] and a skeletonization algorithm for dislocation reconstruction [59].

An Ewald summation method [60] with a radius of 12 Å was used for the calculation of bulk material properties that involved periodic boundary conditions, e.g. lattice parameter, elastic constants and generalized stacking fault (GSF) energies [61]. We used the same short-range interaction cut-off (8 Å) for bulk material properties and nanocompression simulations. GSF energies were computed using the full periodic method described in Gouriet et al. [62] to avoid artefacts induced by charged surfaces. Calculations were

performed along the  $1/2\langle 110 \rangle$  Burgers vector direction for  $\{110\}$ ,  $\{100\}$  and  $\{111\}$  planes. Simulation cells were chosen large enough, especially along the orientation of the stacking fault normal, to reduce the interactions between fault periodic replicas and minimize long-range Coulombic effects. The initial size of the simulation cells are  $1.79 \text{ nm} \times 1.69 \text{ nm} \times 14.29 \text{ nm}$ ,  $1.79 \text{ nm} \times 1.79 \text{ nm} \times 14.31 \text{ nm}$  and  $1.49 \text{ nm} \times 1.55 \text{ nm} \times 27.71 \text{ nm}$  respectively for  $\{110\}$ ,  $\{100\}$  and  $\{111\}$  GSF calculations.

### 3. Results

#### 3.1. Mechanical behavior of MgO nanocubes

The mechanical response of a 140 nm edge size MgO nanocube is displayed in Fig. 2a. The compression test is composed of five successive load–unload cycles. In addition to the stress–strain curve, four on-the-fly images are presented Fig. 2b–e for true strain of about  $\varepsilon = 1.2\%$ ,  $\varepsilon = 18.7\%$ ,  $\varepsilon = 49.7\%$  and  $\varepsilon = 78.9\%$ , respectively. The sample is deformed up to  $\varepsilon = 79.0\%$  before final unload.

Early in the first cycle, the stress–strain dependency is nonlinear and noisy. This transitory stage reflects the accommodation regime between the substrate, the sample and the tip up to  $\varepsilon = 3.5\%$ . Then, the curve exhibits an elastic-like behavior up to  $\varepsilon = 9.0\%$  and a true stress of about  $\sigma = 0.78 \text{ GPa}$ . A Young's modulus of about  $E_{[001]} = 141.9 \text{ GPa}$  is deduced from the early beginning of the first unload. From this point and during the rest of

the whole compression test, mobile contrast bands are observed in the nanocube.

Contrast bands may occur for several reasons, e.g. the elastic deformation of the lattice or the presence of mobile/sessile dislocations. In the following, we will focus only on contrast bands that are believed to be the signature of dislocations. These contrast bands may be recognized by their peculiar curved shape as well as their specific orientation, e.g. the two angled contrast bands observed on the  $\varepsilon = 18.7\%$  image of Fig. 2. Nevertheless, due to the Bragg conditions, all the defects cannot be observed during the experiment.

One can note that all the residual contrasts accumulated during the first load cycle, up to  $\varepsilon = 13.1\%$ , vanish during the first unload. This phenomenon occurs because of both the compressive stress relaxation and the surface image forces, believed to be particularly effective in nanometer-sized samples. This leads to a perfectly refreshed microstructure comparable to the one observed in Fig. 2b.

At  $\varepsilon = 18.7\%$ , one may see two freshly nucleated, linear and parallel contrast bands (Fig. 2c). These bands are tilted  $\sim 45^\circ$  from the  $[001]$  nanocube surfaces, which might be evidence for dislocation glide in  $\{110\}$  slip planes. After their emergence from a surface and/or an edge (the quasi-two-dimensional conditions of the experiment precluding a more precise investigation), both traces escape from the opposite side of the nanocube. Further contrast bands can be observed during the third cycle and the beginning of the fourth one where the true stress rises up to  $\sigma = 1.51 \text{ GPa}$ . During the fourth cycle, successive strain bursts take place. Similar strain bursts are often described in the literature [63–66] and are attributed to dislocation nucleation or multiplication peaks and subsequent severe sudden plastic deformation. Although the deformed nanocube becomes very thick during the fourth cycle, these severe plastic deformation events are still recognizable by the high contrast they produce, e.g. on the  $\varepsilon = 49.7\%$  image (Fig. 2d). Nevertheless, it is not possible to quantitatively analyze slip contrasts from the middle of cycle four up to the end of the fifth cycle because of their high density (Fig. 2e). Finally, the sample is unloaded after the fifth cycle and a total deformation of about  $\varepsilon = 79.0\%$ . No sign of failure has been observed during the unload.

#### 3.2. Focus on the early stages of deformation

In order to investigate further the elementary mechanisms responsible for the first stages of MgO nanocubes deformation, we performed two supplementary in situ compression tests. Stress–strain curves of 90 and 120 nm edge lengths nanocubes are represented Fig. 3. As the stress–strain curve main features of the  $\sim 100 \text{ nm}$  range MgO nanocube have been described in the previous section, we will focus only on new outcomes in the following.

We observe that both samples are characterized by a strain burst occurring at higher stress than in the case of the 140 nm sample. At this point, true stress is  $\sim 2.72$  and  $5.03 \text{ GPa}$ , respectively, for the 120 and the 90 nm samples. In the inset of Fig. 3, an image of the 120 nm sized nanocube is shown at  $\varepsilon = 7.3\%$  i.e. during the initial strain burst. Once again, we observe an inclined and straight contrast band, tilted at  $\sim 45^\circ$  from the indenter and generated from the surface and/or an edge of the nanocube, similarly to what was observed in the case of the 140 nm sample (Fig. 2).

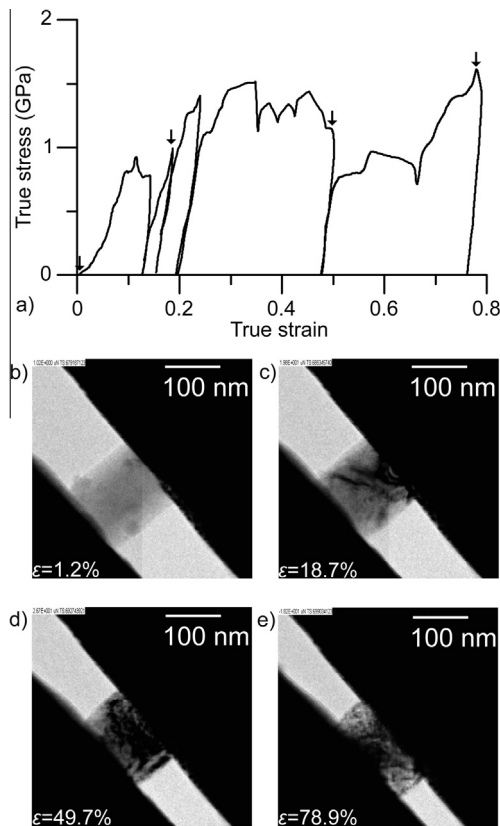


**Fig. 2.** (a) Stress–strain curve for a 140 nm edge lengths MgO nanocube compressed in situ. Five loading–unloading cycles are shown. Black arrows refer to snapshots. (b–e) Images at  $\varepsilon = 1.2\%$ ,  $\varepsilon = 18.7\%$ ,  $\varepsilon = 49.7\%$  and  $\varepsilon = 78.9\%$  true strain are represented.

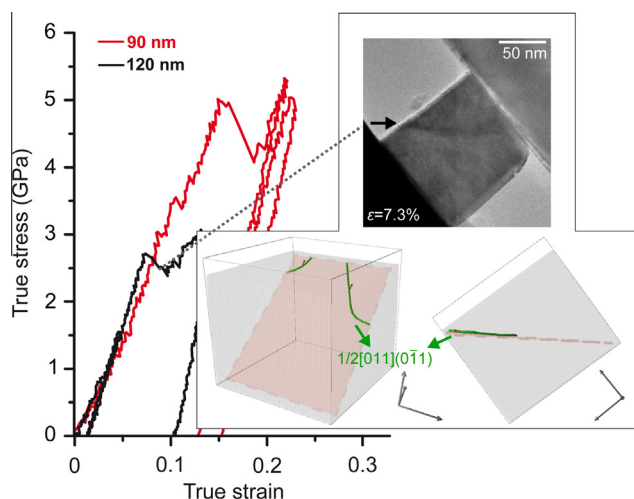


**Fig. 3.** Stress–strain curves for two MgO nanocubes of 90 (red line) and 120 (black line) nm edge lengths. In the inset: TEM image of a 120 nm sample during compression,  $\varepsilon = 7.3\%$ . The black arrow shows a contrast band corresponding to dislocations that emerge from the surface of the cube. Two MD simulation snapshots of a 12.6 nm edge lengths nanocube are also represented. Reconstructed  $1/2\langle 110 \rangle\{110\}$  dislocations are in green. The slip plan is in red. Atoms are shown in transparent light gray for the sake of clarity. The coordinates system is oriented along the cubic directions. (For interpretation of the references to color in this figure legend, the reader is referred to the web version of this article.)

To confirm our hypothesis of  $\{110\}$  glide planes, we performed MD compression tests of MgO nanocubes. Although the compression rate that can be computed is far higher than in the experiment, and the maximum size of the sample is smaller (especially in the case of ionic systems), MD simulations are known to provide a qualitative basis for the identification and interpretation of elementary mechanisms possibly responsible for the deformation of nano-objects [17,67,68]. Fig. 3 shows early nucleated dislocations during the compression of a 12.6 nm edge length nanocube by MD. Here, dislocations are nucleated from two lateral edges (contrarily to the other top and bottom planar edges) of the nanocube. The slip plane is  $(0\bar{1}1)$  and the Nye tensor analysis leads to dislocations characterized by a  $1/2[011]$  Burgers vector.  $1/2\langle 110 \rangle$  Burgers vectors are characteristic of perfect dislocations in the B1 structure. Similar compression tests have been performed for 10.1, 7.6, 5.9 and 4.2 nm edge length cubes. Corresponding stress–strain curves are presented Fig. 4. They are first characterized by a linear elastic regime up to  $\varepsilon \sim 3\%$ .  $E_{[001]}$  values are displayed in Table 1. In order to compare  $E_{[001]}$  to bulk Young's modulus  $E_{[001]}^{Bulk}$ , bulk elastic constants are calculated. Results lead to  $C_{11} = 282.8$  GPa,  $C_{12} = 138.0$  GPa and  $C_{44} = 138.0$  GPa. These results are in good agreement with recent calculations using the same interatomic potential [50]. We deduced  $E_{[001]}^{Bulk} = 192.3$  GPa using the anisotropic elastic theory. Afterwards, the elastic regime becomes non-linear up to  $10.8\% < \varepsilon < 11.4\%$ , depending the size of the sample. This phenomenon is commonly observed at the nanoscale and is attributed to surface forces and anharmonicity [69,70]. The yield stress varies continuously from 40.5 to 35.2 GPa, decreasing the size of the sample, and dislocations nucleate. Nucleation can be inferred from the simulated stress–strain curves by the correlated

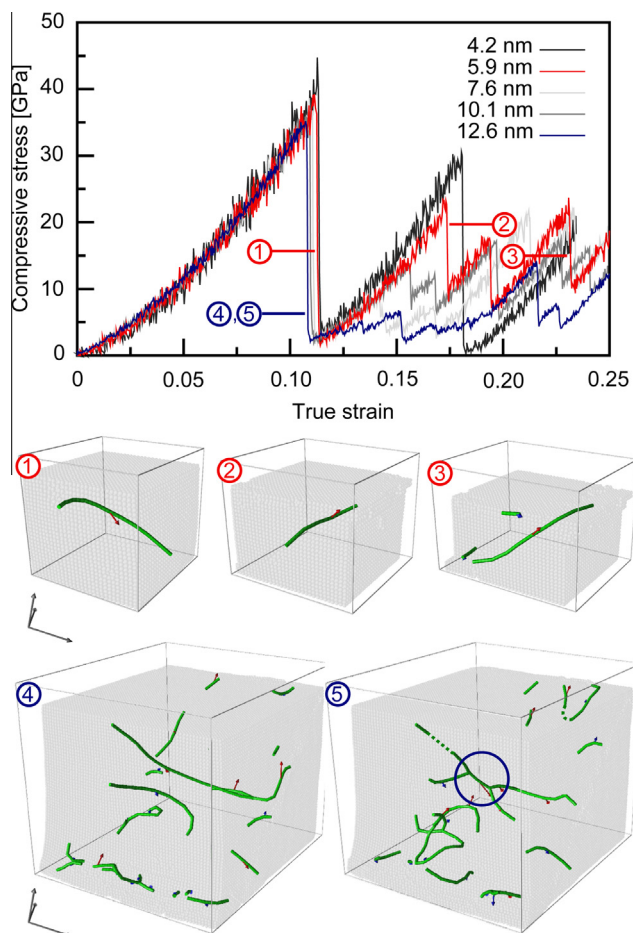


**Fig. 4.** Stress–strain curves of MgO nanocubes from MD compression simulations. ①–⑤: Images of nanocubes during compression. Green lines correspond to dislocations and red arrows represent  $1/2\langle 110 \rangle$  Burgers vector orientation. ①–③ show the evolution of the 5.9 nm sample. ④ and ⑤ show the dislocation organization at the end of the first nucleation peak of the 12.6 nm sample. The blue circle shows a dislocation junction embryo. The coordinates system is oriented along the cubic directions. (For interpretation of the references to color in this figure legend, the reader is referred to the web version of this article.)

stress drops. When dislocations nucleate (or escape), top or bottom surfaces of the sample are rearranged, leading to a slight increase in the distance between the sample top surface and the indenter. As the flat punch force varies inversely with this distance, the stress drops down. The onset of plastic deformation is controlled by  $1/2\langle 110 \rangle\{110\}$  dislocations only, nucleated either from an edge, a surface or a corner of the nanocube. A detailed analysis of the localization of dislocation nucleation first events is summarized in Table 1.

No dislocation is observed in the  $\{100\}$  or  $\{111\}$  glide planes during the simulations. This result is in agreement with early  $45^\circ$  tilted contrast bands, described on the TEM images of Figs. 2 and 3. This confirms that the initial elementary process that governs the deformation of  $\langle 100 \rangle$ -oriented and pristine MgO nanocubes under uniaxial compression is the nucleation of  $1/2\langle 110 \rangle$  perfect dislocations, gliding later in  $\{110\}$  slip planes.

**Table 1.** Young's moduli and yield stresses for MD compression simulations, plus sites and slip systems of the first nucleated dislocations.  $E_{[001]}^{Bulk} = 192.3$  GPa is deduced from the elastic constants and the anisotropic elastic theory. For the 7.6 nm particle, two dislocations nucleate simultaneously.

Size (nm)	$E_{[001]}$ (GPa) ( $E_{[001]}/E_{[001]}^{Bulk}$ )	Yield stress (GPa)	Dislocation slip system	Nucleation site
4.2	142.7 (0.74)	40.5	$\frac{1}{2}[10\bar{1}](101)$	Top edge
5.9	165.0 (0.86)	37.5	$\frac{1}{2}[10\bar{1}](101)$	Bottom corner
7.6	179.2 (0.93)	36.3	$\left\{ \begin{array}{l} \frac{1}{2}[101](\bar{1}01) \\ \frac{1}{2}[011](0\bar{1}1) \end{array} \right.$	Lateral edge Lateral surface
10.1	182.4 (0.95)	35.8	$\frac{1}{2}[101](\bar{1}01)$	Lateral edge
12.5	191.7 (1.00)	34.7	$\frac{1}{2}[011](0\bar{1}1)$	Lateral edge

#### 4. Discussion

Only few in situ compression experiments have been dedicated to ceramic NPs, especially in the 100 nm range size. Here we present results based on a TEM experimental–MD simulation crossed approach, applied to initially dislocation-free MgO nanocubes.

##### 4.1. Toward small-size effects on MgO mechanical properties

In contrast to their bulk counterpart, nanometer-sized MgO particles deform up to large strain, beyond  $\varepsilon = 78.9\%$  in the experiment, and no sign of crack has been observed during and after the compression of the nanocubes. These results apply also in the case of MD compression simulation using the Ball and Grimes interatomic potential. In the simulation, we observe a strong effect of the size decrease on the elastic regime. For particles with size lower than 10 nm edge length,  $E_{[001]}$  decreases, reducing size (Table 1). Furthermore, the elastic regime becomes non-linear. This phenomenon is weaker for larger particles and is thus not expected in the experiments (at least for the sizes we investigate here). Nevertheless,  $E_{[001]}$  is still lower in the experiment ( $\sim 142$  GPa for the 140 nm particle) compared to the experimental bulk value  $E_{[001]}^{Bulk} \sim 248$  GPa [71,72]. We believe that this variation is not a size-effect but may rather be an extrinsic effect as e.g. electron-beam assisted deformation [73–75]. Zheng et al. point out that the force required to deform amorphous silica (a-SiO<sub>2</sub>) NPs at a given elastic strain is lowered by a factor 2 to 3 in the case of electron-beam-on tests compared to electron-beam-off [74]. In the work of Mačković et al., a-SiO<sub>2</sub> NPs are pre-irradiated and then compressed under beam-on/off conditions. Results show that the Young's modulus is increased by a factor 2 (whatever the conditions) compared to the low-dose/beam-off reference conditions with a maximum load force of 50% up to 500% the original one [73]. Similar observations have been made by Zhang et al. in crystalline zinc tin oxide NWs where electron-beam irradiation is believed to change elastic and electrical conductivity properties [75]. Nevertheless, despite the fact that similar processes might influence the Young's modulus in our experiments, we believe that they should not modify the elementary mechanisms responsible for plastic deformation.

While we have performed several compression tests, only perfectly aligned and homogeneously deformed samples are presented here. Therefore, alignment should not be a strong source of bias. Furthermore, we did not notice any significant influence of the aspect size variation, during the deformation of the 140 nm sample, on the subsequent

elastic reloads. As a corollary, no effect of the beam exposure time has been deduced from the analysis of elastic reloads. The aspect size effect on the subsequent elastic portions observed in the simulations has also been investigated without significant outcome. More details about this analysis are provided in the [Supplementary information](#). Finally, the flow stress is also influenced by downscaling, and raises up in comparison to bulk  $\langle 100 \rangle$ -compression tests at RT i.e. from  $\sim 50$  MPa in bulk conditions [24,26,27,76] up to the GPa range for the nanocubes (Figs. 2 and 3). These results confirm that lowering the scale permits an increase in both strength and ductility, even for originally brittle ceramics. More specifically, yield stresses from experiments and simulations seem to exhibit a size-effect of  $\sim 10$  and 100 nm. However, the number of experiments should be increased, as the investigated range of size, to get a more significant statistic and further strengthen this hypothesis. In the following, we will further focus on the special features of the plastic deformation regime of MgO NPs.

##### 4.2. Dislocation nucleation and slip systems in nanosized MgO

Both in situ TEM compression tests and MD simulations agree that  $\{110\}$  dislocations are responsible for plastic deformation in the MgO nanocubes. MD compression simulations lead to full  $1/2\langle 110 \rangle$  Burgers vectors. Neither dislocations in the  $\{100\}$  or  $\{111\}$  slip planes nor twinning dislocations were observed in both the experiments and the simulation.  $1/2\langle 110 \rangle\{110\}$  dislocation glide is also one known mechanism responsible for the deformation of MgO micropillars [77,78] and bulk single crystals [24,26,38,76,79]. Indeed, for  $\langle 100 \rangle$ -compressions, only  $1/2\langle 110 \rangle\{110\}$  and  $1/2\langle 110 \rangle\{111\}$  slip system families may contribute to the deformation. The Schmid factor for these slip system families is about  $m_{\{110\}} = 0.50$  for 4 over 6  $1/2\langle 110 \rangle\{110\}$  slip systems and  $m_{\{111\}} = 0.41$  for 8 over 12  $1/2\langle 110 \rangle\{111\}$  slip systems, others being null. Although both slip system families exhibit comparable Schmid factors,  $1/2\langle 110 \rangle\{111\}$  slip is unfavored due to charge repulsion between ions in the case of NaCl-type ionic materials as MgO [80]. This phenomenon leads to a surprisingly high shear stress for the  $\{111\}$  slip planes compared to what is generally observed, e.g. in fcc metals. With this orientation,  $\{100\}$  slip can only occur in the case of misorientations or local rotations. Nevertheless,  $1/2\langle 110 \rangle\{100\}$  slip is believed to be effective under a rather higher shear stress than  $1/2\langle 110 \rangle\{110\}$  in RT compression experiments [25,27,79], which does not make  $\{100\}$  slip planes suitable candidates to accommodate deformation in our study.

Although the yield strength in the MD simulations (Fig. 4) is obviously influenced by the strain rate dependence of dislocation nucleation from the surfaces [67], the role of  $1/2\langle 110\rangle\{110\}$  dislocations during the compression of MgO nanocubes is most probably strain-rate-independent and further constrained by energetic considerations.

To further investigate the relative role of  $\{100\}$ ,  $\{110\}$  and  $\{111\}$  glide planes, we have calculated GSF energies using the same interatomic potential as that for the MD compression simulations. GSF energies are computed by simply shifting the atoms contained in the upper half of a simulation cell relatively to its lower half by an appropriate translation vector owned by the boundary plan. GSF energies provide a good estimate of the sensitivity of a slip plane to be sheared in a given direction. This concept is frequently used to discuss dislocation-based elementary processes as dislocation core spreading through Peierls–Nabarro approaches [61,81,82] or dislocation nucleation [83–85]. As shown in e.g. Carrez et al. [86], GSF energies calculated in the  $\{110\}$  and the  $\{100\}$  planes of MgO do not exhibit the characteristic, “fcc-like”, stable stacking fault energy (sSFE) that allows  $1/2\langle 110\rangle$  undissociated dislocations only. This corroborates the results inferred from the Nye tensor analysis during the MD compression simulations where perfect dislocations only are observed (Figs. 3 and 4). Conversely, unstable stacking fault energies (uSFEs) can be computed along the Burgers vector direction. The uSFE increases up to a maximum value  $uSFE^{max}$  reached for a displacement equivalent to the half of the Burgers vector length (i.e.  $1.49 \text{ \AA}$ ). Here we find  $uSFE_{\{110\}}^{max} = 916.7 \text{ mJ m}^{-2}$ ,  $uSFE_{\{100\}}^{max} = 2073.1 \text{ mJ m}^{-2}$  and  $uSFE_{\{111\}}^{max} = 2309.4 \text{ mJ m}^{-2}$ .  $uSFE_{\{110\}}^{max}$  and  $uSFE_{\{100\}}^{max}$  are comparable to ab initio calculations and recent molecular statics simulations using the same interatomic potential [50,86]. While the difference between sSFE and uSFE is often used as an energetic criterion to justify preferred dislocation-based nucleation processes (i.e. partial dislocation, perfect dislocation or twinning) in fcc metallic nano-objects [83], we believe that in the strict case of perfect dislocation, the height of the energetic barrier to produce an elementary shear equal to the Burgers vector (i.e. the  $uSFE^{max}$ ) is a good estimate of the slip plane sensitivity to dislocation nucleation. Here we show that  $uSFE_{\{110\}}^{max} < uSFE_{\{100\}}^{max} < uSFE_{\{111\}}^{max}$ , which confirms the occurrence of  $1/2\langle 110\rangle\{110\}$  dislocations, and the lack of  $1/2\langle 110\rangle\{111\}$  dislocations in the MD compression simulations of MgO nanocubes, and thus possibly in the in situ TEM experiments. Finally, one can note that  $uSFE^{max}$  values are one to two orders of magnitude higher in MgO than the sSFE–uSFE range commonly reached in standard fcc metals i.e. in the range of  $10\text{--}100 \text{ mJ m}^{-2}$  [87–89], which might support the extremely high strength observed on the simulated stress–strain curves (Fig. 4).

#### 4.3. Deformation regimes and dislocation network

While the nucleation process and the propagation of  $1/2\langle 110\rangle\{110\}$  dislocations are at the onset of plastic deformation of initially pristine MgO nanocubes, it is interesting to see if dislocation networks occur. Fig. 5 shows four supplementary TEM images of the 140 nm nanocube (already described previously) during the first load cycle. In this figure, one can identify at least two mechanisms that operate simultaneously. Indeed, red lines on Fig. 5 emphasize a

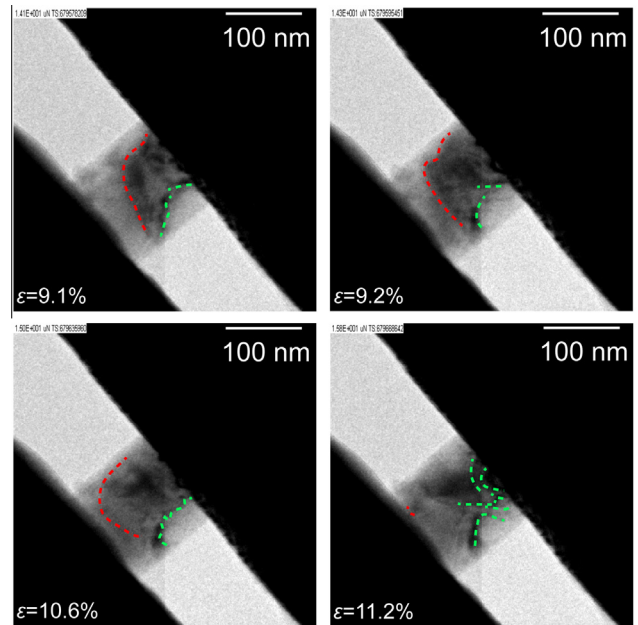


**Fig. 5.** TEM images of a 140 nm MgO nanocube during the first cycle of load. Dashed red lines show a contrast band that escapes progressively the sample. Green lines show an arrangement of contrast bands that are attributed to the formation of a dislocation network. (For interpretation of the references to color in this figure legend, the reader is referred to the web version of this article.)

contrast band that escapes progressively the sample from the surface, just after it nucleates from the other side of the sample. This process of nucleation–exhaustion of dislocations is often observed when dislocation glide is not precluded [10,63]. In some cases, it can be the unique rate-controlling mechanism e.g. in the MD compression simulations for nanocube edge lengths size lower than 10 nm shown Fig. 4. Indeed, for the 4.2 nm and the 5.9 nm edge lengths simulated samples, stress–strain curves clearly show consecutive stress drops. These peaks are due to the nucleation of one or very few dislocations that induce localized deformation and directly escape from the cube after their nucleation, as observed in Fig. 4. This dislocation starvation process is less pronounced in the 7.9 nm edge length sample and disappears nearly from the 12.6 nm sample. Actually, in the case of the 12.6 nm sample, deformation is homogeneous and dislocations nucleate from multiple slip systems during the first stress drop. In this case, gliding dislocations intersect and react, which can be viewed as the critical step of the dislocation network formation (Fig. 4). This process is strongly different from the dislocation starvation process described above, as it does not require further dislocation nucleation, i.e. dislocations later unlock from the dislocation network and multiply to accommodate further deformation.

One should note that the lack of subsequent large stress drops on the 12.6 nm sample stress–strain curve is due not only to this last microstructural process but also to the increase of the sample size. Indeed, following a simple first order approach, one can approximate the average shear  $\bar{\gamma}$  produced by a  $\{110\}$  gliding dislocation in a cube of edge length  $l$  by Eq. (1):

$$\bar{\gamma} = b \frac{\bar{S}}{V} = b \frac{\sqrt{2}}{2l} \quad (1)$$

where  $b$  is the Burgers vector length,  $\bar{S}$  is the averaged  $\{110\}$  surface area swept by the dislocation and  $V$  is the volume of the sample. From Eq. (1), the amount of shear produced by a dislocation decreases as the size of the nanocube increases. As a consequence, and assuming a constant strain rate, the stress response to a shear increment will be smoother for large samples than for a small one.

The two deformation regimes described above and their respective transition have already been observed in metallic nano-objects [10,90], and apply thus also to B1-structured ceramics. Further simulations e.g. discrete dislocation dynamics simulations (DDD) [65,91,92], performed at lower strain rates and applied to larger nanocubes should improve our understanding of the effective deformation processes that operate during in situ TEM compression tests of MgO nanocubes.

Finally, clear signs of curved dislocations occur during the in situ TEM compression tests as in the MD compression simulations. These results are in contradiction with RT TEM observations performed in bulk MgO after compression [33], where dislocation patterns consist merely in long, straight and screw dislocation segments, characteristic of a Peierls lattice friction regime. As the Peierls stress (stress necessary to generate dislocation glide at 0 K) is  $\sim 150$  MPa in the  $\{110\}$  slip planes and 1600 MPa in the  $\{100\}$  in MgO [27,76,79,86], we believe that the lattice friction is overcome in both the experiments and in the simulations of MgO nanocubes, leading to more isotropic dislocation lines.

This topological property is of primary importance because contact reactions between straight screw dislocations may sometimes not lead to the formation of junction locks. This particularly applies in the case of the bcc structure [93] and for the B1 structure of MgO as shown in recent DDD simulations [39]. Actually, non-screw dislocations are required to generate a dislocation junction in MgO. Fig. 4 shows images of a 12.6 nm nanocube deformed in MD simulations where two curved dislocations with  $60^\circ$  tilted Burgers vectors react to create a junction embryo following the reaction path  $1/2[10\bar{1}](101) + 1/2[01\bar{1}](011) \rightarrow 1/2[11\bar{2}](\bar{1}10)$ . This local interaction process is not observed in smaller samples where all the deformation is accommodated by only a few dislocations that never intersect (Fig. 4). This result confirms that the probability of dislocations intersecting is more likely in larger samples due to a higher number of defects. Finally, one can see in Fig. 4 that contact interactions between dislocations (e.g. junctions, crossed or repulsive states) enhance the build-up of a dislocation network during the deformation of the 12.6 nm nanocube.

In summary, and contrary to what is observed in bulk MgO at RT, the high stress reached during the nanocompression tests could allow dislocations to overtake the lattice friction and thus increase the possibility of contact reactions between dislocations. This process improves the formation of a dislocation network, as it is observed in the compression simulations of the 12.6 nm nanocube (Fig. 4). We believe that a similar process is likewise the source of the persistent contrast bands observed during the in situ TEM compression tests (Figs. 2 and 5).

#### 4.4. Implications for NC ceramics

The results presented above have direct potential future impact for the processing (i.e. compaction, ball milling) or the design (i.e. mechanical properties) of nanostructured bulk ceramics. Indeed, knowing the plastic deformation

mechanisms and mechanical constitutive laws of ceramic NPs are of key importance for phenomena such as third body wear particle in contact mechanics, milling of NPs which may exhibit a plastic behavior below a certain size or particle compaction during green body preparation of ceramics. It is for example usually considered that ceramic nanopowders just rearrange without plasticization during compaction [94]. The results presented here for MgO nanocubes and previously for transition alumina nanospheres [14,21] prove that wide plastic flow of ceramic NPs can occur during compaction at RT. This propensity to plastic deformation during compaction opens a new route to deformable ceramics, even at RT. In other words, it would be possible to use plastic deformation of ceramic NPs to obtain green bodies with very high densities and small pores, and sinter them at temperatures well below the ones currently used [95]. Sintering at much lower temperatures would then keep the nanoscale specificities after all the process chain, leading to higher mechanical or peculiar functional properties. This might then apply to orthopedic devices, with ceramics exhibiting high wear and crack resistance, but also for transparent polycrystalline ceramics for which the quest is today to reach the highest density with the smallest grains [96].

## 5. Conclusion

In summary, we have investigated the mechanical behavior of  $\langle 100 \rangle$ -oriented and initially dislocation-free MgO nanocubes using original in situ TEM compression tests in the 100 nm size range and MD simulations. Results show high strength as homogeneous and wide deformation without failure. The analysis of TEM contrast bands suggests possible  $\{110\}$  slip. These results are confirmed by the MD compression simulations, in which the nucleation of  $1/2\langle 110 \rangle\{110\}$  perfect dislocations is at the onset of the plastic deformation. Schmid factor analysis and considerations based on GSF energy calculations consolidate these results. Dislocations nucleate from edges, corners or surfaces of the nanocubes. Contrary to what is observed in bulk MgO single crystals at RT, dislocations are curved in both the experiment and the simulation, which is due the high stress experienced by the sample during the nanocompression test. This property could enhance the formation of a dislocation network that is generally a high-temperature-like process in bulk MgO. Additional simulations and experiments under WBDF diffraction conditions will be conducted to further confirm these results.

## Acknowledgements

The authors thank Dr Philippe Carrez, Dr Vincent Garnier and Dr Christoph Begau for useful discussions. The authors acknowledge the Centre Lyonnais de Microscopie (CLYM) for the access to the JEOL 2010F microscope. This work was granted access to the HPC resources of the FLMSN, “Fédération Lyonnaise de Modélisation et Sciences Numériques”, partner of EQUIPEX EQUIP@MESO.

## Appendix A. Supplementary data

Supplementary data associated with this article can be found, in the online version, at <http://dx.doi.org/10.1016/j.actamat.2014.12.001>.

## References

- [1] M.J. Mayo, D.C. Hague, D.J. Chen, Processing nanocrystalline ceramics for applications in superplasticity, *Mater. Sci. Eng. A* 166 (1993) 145–159.
- [2] M.A. Meyers, A. Mishra, D.J. Benson, Mechanical properties of nanocrystalline materials, *Prog. Mater. Sci.* 51 (2006) 427–556.
- [3] R.J. Narayan, P.N. Kumta, C. Sfeir, D.H. Lee, D. Olton, D.W. Choi, Nanostructured ceramics in medical devices: applications and prospects, *JOM* 56 (2004) 38–43.
- [4] J. Chevalier, L. Gremillard, Ceramics for medical applications: a picture for the next 20 years, *J. Eur. Ceram. Soc.* 29 (2009) 1245–1255.
- [5] O. Kraft, P. Gruber, R. Mönig, D. Weygand, Plasticity in confined dimensions, *Annu. Rev. Mater. Res.* 40 (2010) 293–317.
- [6] A.M. Minor, J.W. Morris, E.A. Stach, Quantitative in situ nanoindentation in an electron microscope, *Appl. Phys. Lett.* 79 (2001) 1625.
- [7] F. Östlund, K. Rzepiejewska-Malyska, K. Leifer, L.M. Hale, Y. Tang, R. Ballarini, et al., Brittle-to-ductile transition in uniaxial compression of silicon pillars at room temperature, *Adv. Funct. Mater.* 19 (2009) 2439–2444.
- [8] R. Miller, V. Shenoy, Size-dependent elastic properties of nanosized structural elements, *Nanotech* 11 (2000) 139–147.
- [9] B. Gilbert, F. Huang, H.Z. Zhang, G.A. Waychunas, J.F. Banfield, Nanoparticles: strained and stiff, *Science* 305 (2004) 651–654.
- [10] J. Greer, W. Nix, Nanoscale gold pillars strengthened through dislocation starvation, *Phys. Rev. B* 73 (2006) 245410.
- [11] T.A. Parthasarathy, S.I. Rao, D.M. Dimiduk, M.D. Uchic, D.R. Trinkle, Contribution to size effect of yield strength from the stochasticity of dislocation source lengths in finite samples, *Scripta Mater.* 56 (2007) 313–316.
- [12] S. Korte, W.J. Clegg, Micropillar compression of ceramics at elevated temperatures, *Scripta Mater.* 60 (2009) 807–810.
- [13] P. Howie, S. Korte, W. Clegg, Fracture modes in micropillar compression of brittle crystals, *J. Mater. Res.* 27 (2012) 141–151.
- [14] E. Calvie, L. Joly-Pottuz, C. Esnouf, P. Clement, V. Garnier, J. Chevalier, et al., Real time TEM observation of alumina ceramic nano-particles during compression, *J. Eur. Ceram. Soc.* 32 (2012) 2067–2071.
- [15] C. Shin, H.-H. Jin, W.-J. Kim, J.-Y. Park, Mechanical properties and deformation of cubic silicon carbide micropillars in compression at room temperature, *J. Am. Ceram. Soc.* 95 (2012) 2944–2950.
- [16] W. Mook, C. Niederberger, M. Bechelany, L. Philippe, J. Michler, Compression of freestanding gold nanostructures: from stochastic yield to predictable flow, *Nanotech* 21 (2010) 055701.
- [17] D. Mordehai, S.-W. Lee, B. Backes, D.J. Srolovitz, W.D. Nix, E. Rabkin, Size effect in compression of single-crystal gold microparticles, *Acta Mater.* 59 (2011) 5202–5215.
- [18] R. Maaß, L. Meza, B. Gan, S. Tin, J.R. Greer, Ultrahigh strength of dislocation-free Ni<sub>3</sub>Al nanocubes, *Small* 8 (2012) 1869–1875.
- [19] J. Deneen, W.M. Mook, A. Minor, W.W. Gerberich, C.B. Carter, In situ deformation of silicon nanospheres, *J. Mater. Sci.* 41 (2006) 4477–4483.
- [20] D.D. Stauffer, A. Beaber, A. Wagner, O. Ugurlu, J. Nowak, K.A. Mkhoyan, et al., Strain-hardening in submicron silicon pillars and spheres, *Acta Mater.* 60 (2012) 2471–2478.
- [21] E. Calvie, J. Réthoré, L. Joly-Pottuz, S. Meille, J. Chevalier, V. Garnier, et al., Mechanical behavior law of ceramic nanoparticles from transmission electron microscopy in situ nano-compression tests, *Mater. Lett.* 119 (2014) 107–110.
- [22] C.E. Carlton, P.J. Ferreira, In situ TEM nanoindentation of nanoparticles, *Micron* 43 (2012) 1134–1139.
- [23] S. Takeuchi, H. Koizumi, T. Suzuki, Peierls stress and kink pair energy in NaCl type crystals, *Mater. Sci. Eng. A* 521 (2009) 90–93.
- [24] C. Hulse, J. Pask, Mechanical properties of magnesia single crystals compression, *J. Am. Ceram. Soc.* 43 (1960) 373–378.
- [25] C. Hulse, S. Copley, J. Pask, Effect of crystal orientation on plastic deformation of magnesium oxide, *J. Am. Ceram. Soc.* 46 (1963) 317–323.
- [26] F. Sato, K. Sumino, The yield strength and dynamic behaviour of dislocations in MgO crystals at high temperatures, *J. Mater. Sci.* 15 (1980) 1625–1634.
- [27] C. Barthel, *Plastische anisotropie von Bleisulfid und magnesiumoxid* (Diploma thesis), University of Göttingen, 1984.
- [28] P. Haasen, C. Barthel, T. Suzuki, Choice of slip system and Peierls stresses in the NaCl structure, in: H. Suzuki, T. Ninomiya, K. Sumino, S. Takeuchi (Eds.), *Dislocations in Solids*, University of Tokyo Press, Tokyo, 1985, pp. 455–462.
- [29] C. Tromas, J. Girard, J. Woignard, Study by atomic force microscopy of elementary deformation mechanisms involved in low load indentations in MgO crystals 80 (2000) 2325–2335.
- [30] I. Stretton, F. Heidelbach, S. Mackwell, F. Langenhorst, Dislocation creep of magnesiowüstite (MgO. 8FeO. 2O), *Earth Planet Sci. Lett.* 194 (2001) 229–240.
- [31] L. Li, D. Weidner, J. Chen, M. Vaughan, M. Davis, W. Durham, X-ray strain analysis at high pressure: effect of plastic deformation in MgO, *J. Appl. Phys.* 95 (2004) 8357.
- [32] F. Appel, H. Bethge, U. Messerschmidt, Dislocation motion and multiplication at the deformation of MgO single crystals in the high voltage electron microscope, *Phys. Status Solidi A* 42 (1977) 61–71.
- [33] U. Messerschmidt, *Dislocation Dynamics During Plastic Deformation*, Springer Series in Materials Science, Berlin, 2010.
- [34] S. Ikeno, E. Furubayashi, Dislocation behavior in pure niobium at low temperatures, *Phys. Status Solidi A* 27 (1975) 581–590.
- [35] F. Louchet, L. Kubin, D. Vesely, In situ deformation of bcc. crystals at low temperatures in a high voltage electron microscope dislocation mechanisms and strain-rate equation, *Philos. Mag. A* 39 (1979) 433–454.
- [36] A. Clauer, B. Wilcox, High temperature tensile creep of magnesium oxide single crystals, *J. Am. Ceram. Soc.* 59 (1976) 89–96.
- [37] P. Haasen, U. Messerschmidt, W. Skrotzki, Low energy dislocation structures in ionic crystals and semiconductors, *Mater. Sci. Eng. A* 81 (1986) 493–507.
- [38] S. Copley, J. Pask, Plastic deformation of MgO single crystals up to 1600 C, *J. Am. Ceram. Soc.* 48 (1965) 139–146.
- [39] J. Amodeo, B. Devincere, P. Carrez, P. Cordier, Dislocation reactions, Plastic anisotropy and forest strengthening in MgO at high temperature, *Mech. Mater.* 71 (2014) 62–73.
- [40] T. Duffy, R. Hemley, H. Mao, Equation of state and shear strength at multimegabar pressures: Magnesium oxide to 227 GPa, *Phys. Rev. Lett.* 74 (1995) 1371–1374.
- [41] A. Zerr, R. Boehler, Constraints on the melting temperature of the lower mantle from high-pressure experiments on MgO and magnesiowüstite, *Nature* 371 (1994) 506–508.
- [42] S. Stankic, M. Müller, O. Diwald, M. Sterrer, E. Knözinger, J. Bernardi, Size-dependent optical properties of MgO nanocubes, *Angew. Chem. Int. Ed.* 44 (2005) 4917–4920.
- [43] N. Takahashi, Simple and rapid synthesis of MgO with nanocube shape by means of a domestic microwave oven, *Solid State Sci.* 9 (2007) 722–724.
- [44] R. Heidenreich, Electron reflections in MgO crystals with the electron microscope, *Phys. Rev.* 62 (1942) 291–292.
- [45] D.J.H. Cockayne, I.L.F. Ray, M.J. Whelan, Investigations of dislocation strain fields using weak beams, *Philos. Mag. A* 20 (1969) 1265–1270.
- [46] A. Thölen, Stress fields at boundaries between contacting particles, *J. Mater. Sci.* 41 (2006) 4466–4476.
- [47] R.O. Kagel, Infrared study of the adsorption of methanol and ethanol on magnesium oxide, *J. Chem. Phys.* 49 (1968) 1638.

- [48] S. Plimpton, Fast parallel algorithms for short-range molecular-dynamics, *J. Comput. Phys.* 117 (1995) 1–19.
- [49] G. Henkelman, B. Uberuaga, D. Harris, J. Harding, N. Allan, MgO addimer diffusion on MgO(100): a comparison of ab initio and empirical models, *Phys. Rev. B* 72 (2005) 115437.
- [50] P. Carrez, J. Godet, P. Cordier, Atomistic simulations of  $1/2\langle 110 \rangle$  screw dislocation core in magnesium oxide. *Comp. Mat. Sci.* <http://dx.doi.org/10.1016/j.commatsci.2014.10.019>
- [51] D.J. Hardy, J.E. Stone, K. Schulten, Multilevel summation of electrostatic potentials using graphics processing units, *Parallel Comput.* 35 (2009) 164–177.
- [52] E. Bitzek, P. Koskinen, F. Gähler, M. Moseler, Structural relaxation made simple, *Phys. Rev. Lett.* 97 (2006) 170201.
- [53] W. Hoover, Canonical dynamics: equilibrium phase-space distributions, *Phys. Rev. A* 31 (1985) 1695.
- [54] K. Van Vliet, J. Li, T. Zhu, S. Yip, S. Suresh, Quantifying the early stages of plasticity through nanoscale experiments and simulations, *Phys. Rev. B* 67 (2003) 104105.
- [55] J. Amodeo, C. Begau, E. Bitzek, Sup mat: atomistic simulations of compression tests on Ni<sub>3</sub>Al nanocubes, *Mater. Res. Lett.* (2014) 1–6
- [56] C. Begau, AtomViewer. AtomViewer Free Download at <http://Homepage.uni-Bochum.de/ChristophBegau/>, 2014.
- [57] G. Ackland, A. Jones, Applications of local crystal structure measures in experiment and simulation, *Phys. Rev. B* 73 (2006) 054104.
- [58] C.S. Hartley, Y. Mishin, Characterization and visualization of the lattice misfit associated with dislocation cores, *Acta Mater.* 53 (2005) 1313–1321.
- [59] C. Begau, A. Hartmaier, E.P. George, G.M. Pharr, Atomistic processes of dislocation generation and plastic deformation during nanoindentation, *Acta Mater.* 59 (2011) 934–942.
- [60] P.J. in't Veld, A.E. Ismail, G.S. Grest, Application of Ewald summations to long-range dispersion forces, *J. Chem. Phys.* 127 (2007) 144711.
- [61] V. Vitek, Intrinsic stacking faults in body-centred cubic crystals, *Philos. Mag.* A 18 (1968) 773–786.
- [62] K. Gouriet, P. Carrez, P. Cordier, Modelling [100] and [010] screw dislocations in MgSiO<sub>3</sub> perovskite based on the Peierls–Nabarro–Galerkin model, *Modell. Simul. Mater. Sci. Eng.* 22 (2014) 025020.
- [63] S.H. Oh, M. Legros, D. Kiener, G. Dehm, In situ observation of dislocation nucleation and escape in a submicrometre aluminium single crystal, *Nat. Mater.* 8 (2009) 95–100.
- [64] D. Kiener, A.M. Minor, Source truncation and exhaustion: insights from quantitative in situ TEM tensile testing, *Nano Lett.* 11 (2011) 3816–3820.
- [65] F. Csikor, C. Motz, D. Weygand, M. Zaiser, S. Zapperi, Dislocation avalanches, strain bursts, and the problem of plastic forming at the micrometer scale, *Science* 318 (2007) 251–254.
- [66] M. Uchic, D. Dimiduk, J. Florando, W. Nix, Sample dimensions influence strength and crystal plasticity, *Science* 305 (2004) 986–989.
- [67] T. Zhu, J. Li, A. Samanta, A. Leach, K. Gall, Temperature and strain-rate dependence of surface dislocation nucleation, *Phys. Rev. Lett.* 100 (2008) 025502.
- [68] T. Zhu, J. Li, Ultra-strength materials, *Prog. Mater. Sci.* 55 (2010) 710–757.
- [69] M.T. McDowell, A.M. Leach, K. Gaill, On the elastic modulus of metallic nanowires, *Nano Lett.* 8 (2008) 3613–3618.
- [70] Y.J. Wang, G. Gao, S. Ogata, Size-dependent transition of deformation mechanism, and nonlinear elasticity in Ni<sub>3</sub>Al nanowires, *Appl. Phys. Lett.* 102 (2013) 041902.
- [71] M.A. Durand, The temperature variation of the elastic moduli of NaCl, KCl and MgO, *Phys. Rev.* 50 (1936) 449–455.
- [72] D.-H. Chung, Elastic moduli of single crystal and polycrystalline MgO, *Philos. Mag. A* 8 (1963) 833–841.
- [73] M. Mačković, F. Niekkel, L. Wondraczek, E. Spiecker, Direct observation of electron-beam-induced densification and hardening of silica nanoballs by in situ transmission electron microscopy and finite element method, *Acta Mater.* 79 (2014) 363–373.
- [74] K. Zheng, C. Wang, Y.-Q. Cheng, Y. Yue, X. Han, Z. Zhang, et al., Electron-beam-assisted superplastic shaping of nanoscale amorphous silica, *Nat. Commun.* 1 (2010) 1–8.
- [75] J. Zang, L. Bao, R.A. Webb, X. Li, Electron beam irradiation stiffens zinc tin oxide nanowires, *Nano Lett.* 11 (2011) 4885–4889.
- [76] J. Amodeo, P. Carrez, B. Devincere, P. Cordier, Multiscale modelling of MgO plasticity, *Acta Mater.* 59 (2011) 2291–2301.
- [77] S. Korte, W. Clegg, Discussion of the dependence of the effect of size on the yield stress in hard materials studied by microcompression of MgO, *Philos. Mag. A* 91 (2011) 1150–1162.
- [78] S. Korte, M. Ritter, C. Jiao, P. Midgley, W. Clegg, Three-dimensional electron backscattered diffraction analysis of deformation in MgO micropillars, *Acta Mater.* 59 (2011) 7241–7254.
- [79] F. Appel, B. Wielke, Low temperature deformation of impure MgO single crystals, *Mater. Sci. Eng.* 73 (1985) 97–103.
- [80] J. Gilman, Plastic anisotropy of LiF and other rocksalt-type crystals, *Acta Metall.* 7 (1959) 608–613.
- [81] R. Peierls, The size of a dislocation, *Proc. Phys. Soc.* 52 (1940) 34–37.
- [82] F. Nabarro, Dislocations in a simple cubic lattice, *Proc. Phys. Soc.* 59 (1947) 256–272.
- [83] H. Van Swygenhoven, P.M. Derlet, A.G. Frøseth, Stacking fault energies and slip in nanocrystalline metals, *Nat. Mater.* 3 (2004) 399–403.
- [84] J. Rice, Dislocation nucleation from a crack tip: an analysis based on the Peierls concept, *J. Mech. Phys. Solids* 40 (1992) 239–271.
- [85] E. Tadmor, S. Hai, A Peierls criterion for the onset of deformation twinning at a crack tip, *J. Mech. Phys. Solids* 51 (2003) 765–793.
- [86] P. Carrez, D. Ferré, P. Cordier, Peierls–Nabarro modelling of dislocations in MgO from ambient pressure to 100 GPa, *Modell. Simul. Mater. Sci. Eng.* 17 (2009), 035010–1521.
- [87] C.R. Weinberger, W. Cai, Plasticity of metal nanowires, *J. Mater. Chem.* 22 (2012) 3277.
- [88] M. Mehl, D. Papaconstantopoulos, N. Kioussis, M. Herbranson, Tight-binding study of stacking fault energies and the Rice criterion of ductility in the fcc metals, *Phys. Rev. B: Condens. Matter* 61 (2000) 4894–4897.
- [89] J.A. Zimmerman, H.J. Gao, F.F. Abraham, Generalized stacking fault energies for embedded atom FCC metals, *Modell. Simul. Mater. Sci. Eng.* 8 (2000) 103–115.
- [90] I. Ryu, W.D. Nix, W. Cai, Plasticity of bcc micropillars controlled by competition between dislocation multiplication and depletion, *Acta Mater.* 61 (2013) 3233–3241.
- [91] B. Devincere, T. Hoc, L. Kubin, Dislocation mean free paths and strain hardening of crystals, *Science* 320 (2008) 1745–1748.
- [92] V.V. Bulatov, L.L. Hsiung, M. Tang, A. Arsenlis, M.C. Bartelt, W. Cai, et al., Dislocation multi-junctions and strain hardening, *Nature* 440 (2006) 1174–1178.
- [93] L. Kubin, R. Madec, B. Devincere, Dislocation intersections and reactions in FCC and BCC crystals, in: H. Zbib, D. Lassila, L. Levine, K. Hemker (Eds.), *Multiscale Phenomena in Materials Experiments and Modeling Related to Mechanical Behavior*, vol. 779, Materials Research Society Symposium Proceedings, Warrendale, PA, 2003, pp. 25–36.
- [94] R. Oberacker, Powder compaction by dry pressing, in: R. Riedel, I. Chen (Eds.), *Ceramics Science and Technology*, Wiley-VCH, Weinheim, 2012, pp. 1–37.
- [95] J. Zheng, J.S. Reed, Effects of particle packing characteristics on solid-state sintering, *J. Am. Ceram. Soc.* 72 (1989) 810–817.
- [96] A. Krell, J. Klimke, T. Hutzler, Transparent compact ceramics: Inherent physical issues, *Opt. Mater.* 31 (2009) 1144–1150.